Future Medical Engineering Based on Bionanotechnology

Proceedings of the Final Symposium of the Tohoku University 21st Century Center of Excellence Program

Sendai International Center, Japan 7 – 9 January 2007

Editors

ESASHI Masayoshi

ISHII Keizo

OHUCHI Noriaki

OSUMI Noriko

SATO Masaaki

YAMAGUCHI Takami

Tohoku University, Japan

ICP

Imperial College Press

Published by

Imperial College Press
57 Shelton Street
Covent Garden
London WC2H 9HE

Distributed by

World Scientific Publishing Co. Pte. Ltd.
5 Toh Tuck Link, Singapore 596224
USA office: 27 Warren Street, Suite 401-402, Hackensack, NJ 07601
UK office: 57 Shelton Street, Covent Garden, London WC2H 9HE

British Library Cataloguing-in-Publication Data
A catalogue record for this book is available from the British Library.

FUTURE MEDICAL ENGINEERING BASED ON BIONANOTECHNOLOGY
Proceedings of the Final Symposium of the Tohoku University 21st Century Center of Excellence Program

ISBN 1-86094-710-7

Printed in Singapore by Mainland Press

ULTRASONIC CROSS-SECTIONAL IMAGING AND MEASUREMENT OF MOTION AND MECHANICAL PROPERTIES OF ARTERIAL WALLS

HIDEYUKI HASEGAWA[1)], JUN INAGAKI[1)], TAKASHI MASHIYAMA[1)], TAKANORI NUMATA[1)], MASATAKA ICHIKI[2)], FUMIAKI TEZUKA[3)], HIROSHI KANAI[1)]

1) Graduate School of Engineering, Tohoku University, Aoba-ku Aramaki-aza-Aoba 6-6-05, Sendai, 980-8579, Japan

2) Sendai Hospital of East Railway Company, Aoba-ku Itsutsubashi 1-1-5, Sendai, 980-8508, Japan

3) Sendai Medical Center, Miyagino-ku Miyagino 2-8-8, Sendai, 983-8520, Japan

Ultrasound can be used for mechanical property measurements of the arterial wall in addition to imaging of its morphology. This paper describes (1) accurate imaging of the carotid sinus which cannot be assumed to be a straight cylindrical shell, (2) measurement of elasticity and tissue characterization of the arterial wall based on the axial motion estimation, and (3) lateral motion estimation in the carotid artery.

Keywords: imaging of arterial morphology, beam steering, artery motion, elasticity, atherosclerosis.

1. Introduction

Rupture of atherosclerotic plaque is probably the most important factor underlying the sudden onset of the acute coronary syndrome [1]. Direct characterization of the composition and vulnerability of atherosclerotic plaque, rather than measurement of the angiographic lumen [2], may offer insight into the mechanisms of plaque regression and progression [3,4] and thereby promote evaluation of cholesterol-lowering therapy [5,6] for reduction of cardiovascular events.

Diagnostic ultrasound is widely used for morphology imaging of the arterial wall. In clinical observation of the carotid artery with ultrasound, it is difficult to accurately image an artery with atherosclerotic plaque or the carotid sinus because they are not flat and ultrasonic beams does not incident normal to the

wall in the case of conventional linear scanning. This paper describes a method for accurately imaging such targets by steering ultrasonic beams.

For the evaluation of dynamic mechanics, arterial elasticity has been determined by measuring the pulse wave velocity [7] and the rough change in the diameter of the artery [8]. However, the mechanical property of plaque cannot be directly determined by these methods because they evaluate average elasticity of the entire circumference. A method to detect the vulnerability of atherosclerotic plaque with sufficient accuracy has not yet been reported. The purpose of the present study was to determine the regional elasticity of the arterial wall and tissue characterization. At the last, arterial motion along in its longitudinal direction, which is lateral to the ultrasound beam, was measured.

2. Methods

2.1. *Beam steering for accurate B-mode imaging* [9]

Figure 1 shows a schematic diagram of the beam steering. The ultrasonic beam scans M positions along the x-axis by conventional linear scanning. The depth of the arterial wall, y_i (i =1, 2, ..., M), at each beam position, x_i (i =1, 2, ..., M), is manually predetermined in the B-mode image obtained by conventional linear scanning. The interval between the neighboring ultrasonic beams is defined by $\Delta x = x_{i+1} - x_i$. With respect to each position, (x_i, y_i), of the i-th ultrasonic beam on the wall, a regional slope, $a_{w,i}$, of the arterial wall to the surface of the ultrasonic probe is estimated by the least-squares method using positions, $\{(x_i, y_i)\}$, of neighboring $\pm N$ ultrasonic beams on the arterial wall, as follows:

$$a_{w,i} = \frac{(2N+1)\sum_{i=-N}^{N} x_i \cdot y_i - \left(\sum_{i=-N}^{N} x_i\right)\left(\sum_{i=-N}^{N} y_i\right)}{(2N-1)\sum_{i=-N}^{N} x_i^2 - \left(\sum_{i=-N}^{N} x_i\right)^2}. \tag{1}$$

From the estimated $a_{w,i}$, the slope, a_i, and the angle, θ_i, of the beam that is perpendicular to the arterial wall at (x_i, y_i) are determined as follows:

$$a_i = -\frac{1}{a_{w,i}}, \tag{2}$$

$$\theta_i = \tan^{-1} a_i. \tag{3}$$

From the determined θ_i (rad) and the (x_i, y_i) of the arterial wall, the center, b_i, of the aperture that transmits an ultrasonic beam to (x_i, y_i) is given by

$$b_i = x_i - \frac{y_i}{\tan\theta_i} = x_i - \frac{y_i}{a_i}. \quad (4)$$

By determining θ_i and b_i (mm) for all positions, $\{(x_i, y_i)\}$, on the wall, all beams are designed to be perpendicular to the arterial wall.

In this study, θ_i is assigned in discrete values. Therefore, the discrete beam angle, θ'_i , that is the nearest to θ_i is selected from pre-assigned angles of K beams. The b_i of the aperture is calculated again using θ'_i. The b_i of the aperture should be also assigned in a discrete value that depends on the element pitch of the ultrasonic probe. The discrete transmit position, b'_i, of the aperture, which is nearest to b_i, is selected, as well as θ'_i. In this way, the ultrasonic beam is transmitted to the position, (x'_i, y'_i), on the wall as perpendicular as possible. Although the designed ultrasonic beam does not exactly pass through the (x_i, y_i) because of the discrete values of b'_i and θ'_i, the difference, $|x'_i - x_i|$, is less than half the element pitch.

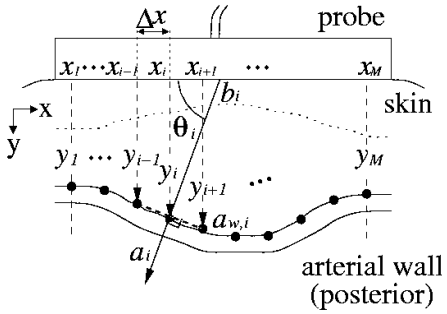

Fig. 1. Determination of optimum beam position and angle (N = 1).

2.2. *Elasticity estimation and tissue characterization based on axial motion estimation*

2.2.1. *Axial motion estimation by "phased tracking method"* [10]

An ultrasonic beam was sequentially scanned at M positions with a linear-type ultrasonic probe of 7 MHz using conventional ultrasound diagnostic equipment (Toshiba SSH-140A), and multiple (N_m+1) points were preset from the luminal surface to the adventitia along the m-th ultrasonic beam (m=1, …, M) with constant intervals of h_0=375 μm at a time t_0 just before the ejection period. By dividing the arterial wall into multiple layers, we defined the n-th layer (n =1, …,

N_m) as being between two contiguous points, n and n+1, along each beam. For measurement of the change in thickness of each of the N_m layers, the instantaneous depth $x_{m,n}(t)$ of the n-th point along the m-th beam was simultaneously tracked by applying the *phased tracking method* [10] to the received ultrasound. The minute decrease of several tenths of a micrometer in thickness of the n-th layer resulting from the arrival of the pressure wave at the beginning of the ejection period was determined by $\Delta h_{m,n}(t) = x_{m,n+1}(t) - x_{m,n}(t) - h_0$.

2.2.2. *Radial strain and elasticity estimated by axial displacements*

From the ratio of the maximum decrease in thickness during one heartbeat, $\Delta h_{m,n,\max}=\max_t|\Delta h_{m,n}(t)|$, to the initial thickness, h_0, of the n-th layer, the maximum deformation of the n-th layer was obtained by $\Delta\varepsilon_{m,n,\max}=\Delta h_{m,n,\max}/h_0$. Since the deformation was sufficiently small and was in the linear regime, it showed incremental strain in the radial direction. By assuming that the arterial wall is incompressible and that the blood pressure is applied normal to each layer, the elastic modulus of the n-th layer along the m-th beam, $E_{\theta,m,n}$, is approximately given by [11]

$$E_{\theta,m,n} \cong \frac{1}{2}\left(\frac{\rho_{m,n,0}}{h_0}+\frac{N_m-n+1}{N_m}\right)\frac{\Delta p}{\Delta\varepsilon_{m,n,\max}} \quad (n=1,\ldots,N_m;\, m=1,\ldots,M), \tag{5}$$

where $\rho_{m,n,0}$ is the initial inner radius of curvature of the n-th layer along the m-th beam at time t_0. We assumed that the pressure in the arterial wall decreases linearly with the distance from the intimal side to the adventitia and that the arterial wall is almost isotropic.

For the region with a length of 18 mm (M = 60) along the axis of the artery, the regional elasticity $E_{\theta,m,n}$ was estimated on the cross-sectional image. Since the reflected ultrasound was received at a sampling interval of 100 ns (=75 μm along depth direction) after the quadrature demodulation, we further divided each layer with a thickness of h_0 into 5 points, shifted the initial depth of each layer by 1/5 of h_0 and applied the above procedure to each depth. Thus, $E_{\theta,m,n}$ was estimated at intervals of 75 μm in the depth direction and 300 μm in the longitudinal direction of the arterial wall.

2.2.3. *Arterial tissue characterization based on elasticity* [12-14]

In this study, an elasticity image is classified using the likelihood function L_i (i=1: lipid, 2: blood clot, 3: fibrous tissue, 4: calcified tissue) of the elasticity

distributions. To obtain the likelihood function of the elasticity distribution of each tissue, the elasticity distribution is translated using the normal distribution to obtain the probability distribution. From *in vitro* experiments, the elasticity distribution of each tissue, i, is obtained as illustrated in Fig. 2(a). The elasticity distribution of each tissue consists of J_i data points with respective elastic moduli (i =1: lipid, 2: blood clot, 3: fibrous tissue, 4: calcified tissue). Using all data of J_i points (J_1: 425, J_2: 301, J_3: 5979, J_4: 579) with respective elastic moduli, the ascending sequence is made for each tissue, i, as shown in Fig. 2(b). In this sequence, the j-th datum (j=1, ..., J_1) has the corresponding elastic modulus E_j (E_j<E_{j+1}) where j is named the elasticity number. It is clear in Fig. 2(a) that the mean elastic modulus of the distribution is largely different from the elastic modulus of the (J_i /2)-th datum at the center of the ascending sequence. One of reasons for this is considered as follows: To obtain the elastic modulus, the change in the thickness (radial strain) of the arterial wall due to a heartbeat is measured using ultrasound. The measured change in thickness is expressed by the sum of the actual change in thickness Δh and noise e of the measurement system, and the elastic modulus is proportional to the reciprocal $1/(\Delta h+e)$ of the measured change in thickness. Therefore, the variance of the estimated elastic moduli increases with decreasing actual change in thickness (increasing elastic modulus) in comparison with the case of increasing change in thickness (decreasing elastic modulus). As a result, the elasticity distribution is broadened at a high elastic modulus. Thus, as shown in Fig. 2(c), the normal distribution is assumed with respect to the elasticity number j so that the probability around the center of the ascending sequence made becomes the maximum.

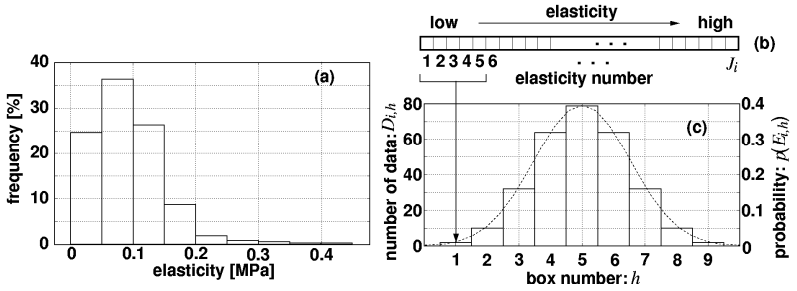

Fig. 2. Illustration of allocation of elasticities of elasticity distribution to boxes of normal distribution. (a) Original elasticity distribution of the tissue. (b) Ascending sequence of elastic modulus of elasticity distribution. (c) Probability distribution obtained using normal distribution.

The probability distribution of each tissue was obtained by allocating all the data of J_i points of each tissue i to boxes of the normal distribution. The number

of boxes, $\{B_i\}$, of the normal distributions is determined so that the number of data in the box for a box number, which is located at threefold the standard deviation of the box number from the mean (mean ± 3×SD), becomes one. As shown in Fig. 2(c), the number of data, $D_{i,h}$ (h=1, ..., B_i), included in each box is determined by following the line of the normal distribution. Then, the (J_i/2)-th datum is included in the box with the highest probability. By allocating all the data of J_i points of each tissue to boxes of the corresponding normal distribution, the mean elasticity $\bar{E}_{i,h}$ of the data included in each box is obtained.

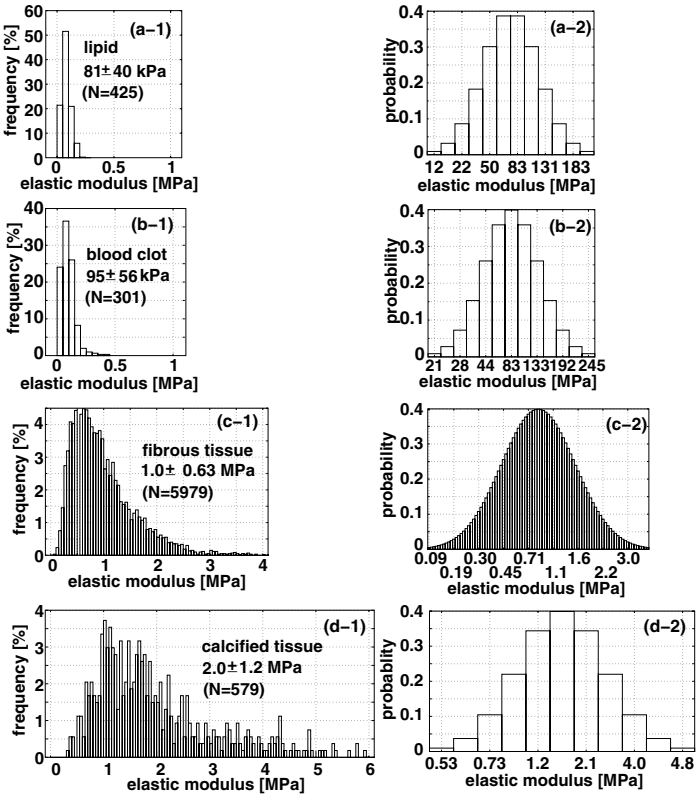

Fig. 3. Elasticity distribution and probability distribution of each tissue. (a) Lipid, (b) blood clot, (c) fibrous tissue, and (d) calcified tissue.

Figures 3(a-1), 3(b-1), 3(c-1), and 3(d-1) show the elasticity distributions for lipids, blood clots, fibrous tissue, and calcified tissue, respectively, and Figs. 3(a-2), 3(b-2), 3(c-2), and 3(d-2) show the respective probability distributions, p_i ($\bar{E}_{i,h}$), whose horizontal axis was labeled by the mean elasticity $\bar{E}_{i,h}$ of the

corresponding box $B_{i,h}$. When the elastic modulus $E_{m,n}$ measured at depth n along the m-th ultrasonic beam is closest to the mean elasticity $\bar{E}_{i,h}$ of the box $B_{i,h}$, the probability $p'_i(E_{m,n})$ with respect to the elastic modulus $E_{m,n}$ was determined to be $p_i(\bar{E}_{i,h})$. For each pixel with the corresponding elastic modulus $E_{m,n}$, the region of interest (ROI) $R_{m,n}$ of ±450 mm in the depth direction and ±450 mm in the longitudinal direction of the artery is assigned. Thus, there are up to 36 elastic moduli in the ROI. Using the probability distribution $p'_i(E_{m,n})$, the log likelihood function $\ln(L_i)$ for the i-th class is obtained with respect to elasticities in $R_{m,n}$ as

$$\ln L_i = \sum_{(k,l)\in R_{m,n}} \ln p'_i(E_{k,l}). \tag{6}$$

However, the size of an ROI varies at the edge of an elasticity image. Therefore, we employ the log likelihood function normalized by the number of elasticities in an ROI. Thus, all pixels in an elasticity image are classified into the class that has the largest likelihood.

For comparison, the elasticity image is also classified by the Mahalanobis distance between the elasticity value of each single pixel and the elasticity distribution of each tissue (mean±SD: lipids 81±40 kPa, blood clots 95±56 kPa, fibrous tissue 1.0±0.63 MPa, calcified tissue 2.0±1.2 MPa).

2.3. *Lateral motion estimation* [15]

Using an ultrasonic probe of 10 MHz, an ultrasound beam scans the carotid artery in its longitudinal direction at 70 positions with intervals of 0.1 mm. At each position, RF echoes are acquired at a sampling frequency of 40 MHz. Let us define the RF signal at beam position b and depth d in n-th frame. A B-mode image can be constructed with a 2-dimensional (radial-longitudinal of the artery) data set obtained by one scanning, which is called as frame. To reduce the spacing between RF lines, which is a factor limiting the spatial resolution in the measurement of the displacement which is lateral to the ultrasonic beam, K RF lines, $\mathrm{rf}'_n(d,\ b + k/(K+1))$, are interpolated between original RF lines, $\mathrm{rf}_n(d,\ b)$, using the linear interpolation as follows:

$$\mathrm{rf}'_n\left(d, b+\frac{k}{K+1}\right) = \frac{(K+1-k)\mathrm{rf}_n(d,b) + k\cdot \mathrm{rf}_n(d,b+1)}{K+1}. \quad (k=1,2,\ldots,K) \tag{7}$$

Each interval of 2 RF lines is shown by $\Delta x_e(K) = 0.1/(K+1)$ [mm]. Then, the lateral displacement, $x_l(n)$, is estimated using the correlation function, $\gamma(n;\ \Delta m,$

Δl), between two frames including interpolated RF echoes. The correlation function between n-th and (n+ΔN)-th frames including interpolated RF lines is obtained with respect to each axial and lateral shifts, Δm_n and Δl_n, of the region of interest (ROI) in the (n+ΔN)-th frame relative to the position of ROI in the n-th frame. The axial and lateral displacements between n-th and (n+ΔN)-th frames are determined from the axial and lateral shifts, Δm_n and Δl_n, which give the maximum correlation coefficient. In this study, the ROI size is 5.8 mm × 0.2 mm, and the interval for calculating the correlation is 52 ms (ΔN = 10). Δm_n and Δl_n are changed from -0.08 mm to 0.08 mm and from -0.2 mm to 0.2 mm, respectively.

Lateral and axial average velocities, $v_l(n)$ and $v_r(n)$, between n-th and (n+ΔN)-th frames are calculated by lateral and axial shifts, Δl_n and Δm_n, respectively. Lateral and axial displacements, $\Delta x_l(n)$ and $\Delta x_r(n)$, between n-th and (n+1)-th frames are calculated by lateral and axial average velocities $v_l(n)$ and $v_r(n)$. Lateral and axial displacements, $x_l(n)$ and $x_r(n)$, at each frame are estimated by accumulating instantaneous displacements, $\Delta x_l(n)$ and $\Delta x_r(n)$, during a frame interval obtained from average velocities, $v_l(n)$ and $v_r(n)$. The position of ROI in the (n+1)-th frame is determined by the lateral and axial displacements, $x_l(n)$ and $x_r(n)$.

3. Results

3.1. *Accurate B-mode imaging of carotid sinus*

3.1.1. *Basic experiment using a phantom*

The shape of the phantom simulates the arterial wall at the carotid sinus and the phantom has a hollow. The width of the hollow is 15 mm, and the depth is 2.5 mm. The phantom was fixed in a water bath and it was measured using diagnostic equipment (Aloka SSD-6500) with a conventional linear-type ultrasonic probe at 10 MHz. The distance from the surface of the ultrasonic probe to the surface of the phantom was 13 mm. 105 ultrasonic beams with intervals, Δx, of 0.2 mm are transmitted in a frame, and the beam angle, θ'_i, was changed by 2º frame by frame from θ'_i (1)=70º to θ'_i (21)=110º during 21 frames. Therefore, the elapsed time for acquiring the RF data of 21 frames was 165 ms in the case of a frame rate of 127 Hz in this experiment. Ultrasonic RF echoes were acquired at a sampling frequency of 40 MHz. Figure 4(a) shows a B-mode image of the object obtained by conventional linear scanning using 105 ultrasonic beams (θ'_i (11)=90º). The surface of the phantom was manually

assigned at 105 positions $\{(x_i, y_i)\}$ (i =1, 2, ..., 105) on the B-mode image [dotted line in Fig. 4(a)]. The beam, with angle θ_i and transmit position b_i, that is perpendicular to the surface of the phantom was determined using $\{(x_i, y_i)\}$. The yellow lines in Fig. 4(b) show the calculated optimum beams. Then, the beam with θ'_i and b'_i was selected. Figure 4(c) shows a B-mode image constructed from the ultrasonic RF echoes obtained using the calculated beams with $\{(\theta'_i, b'_i)\}$. As shown in the areas surrounded by circles in Fig. 4(a), the surface of the phantom could not be imaged clearly in the areas where the ultrasonic beams incline from a vertical direction by more than 20° as shown in the B-mode image obtained by conventional linear scanning. On the other hand, strong reflected echoes were obtained in such areas using the proposed method, and the phantom was imaged over the entire scanned area, as shown in Fig. 4(c).

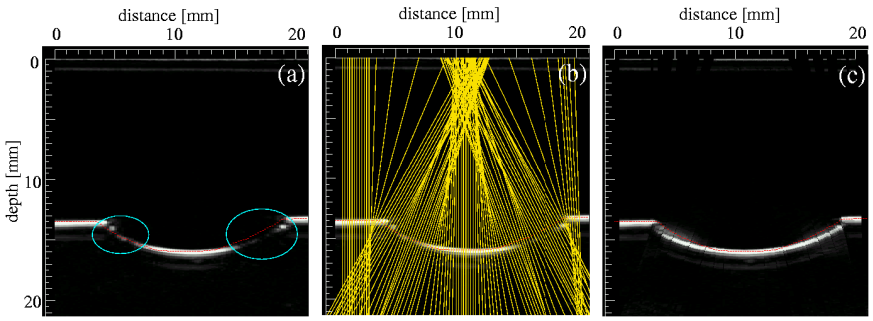

Fig. 4. (a) B-mode image obtained by conventional linear scanning (red line: assigned silicone surface). (b) Calculated beams (yellow lines) superimposed on B-mode image. (c) B-mode image obtained by proposed method.

3.1.2. In vivo *measurement at a carotid artery*

A human common carotid sinus of a 25-year-old male was measured in the long-axis plane. To reduce the elapsed time for acquiring RF data, ultrasonic beams were transmitted every 5° from $\theta'_i(1)$=70° to $\theta'_i(9)$=110° and discrete steered angles, $\{\theta'_k\}$, were changed frame by frame during nine frames. Ultrasonic RF data were acquired during nine frames (82 ms at a frame rate of 110 Hz) just before the time of the R-wave of the electrocardiogram. Figure 5(a) shows a B-mode image obtained by conventional linear scanning, composed of 105 ultrasonic beams with intervals, Δx, of 0.2 mm ($\theta'_i(5)$=90º). The red line in Fig. 5(b) shows the assigned (x_i, y_i) of the posterior wall, and the yellow lines in Fig. 5(b) show the calculated optimum beams. Figure 5(c) shows a B-mode image constructed from the ultrasonic RF echoes obtained using the calculated beams with $\{(\theta'_i, b'_i)\}$. As shown by the area surrounded by a circle in Fig. 5(a),

the intima-media complex could not be imaged clearly by conventional linear scanning in the area where the ultrasonic beams incline from the perpendicular direction relative to the wall by more than 2.5º. However, sufficient reflected echoes were obtained from such an area using the proposed method, and the intima-media complex was almost imaged over the entire scanned area as shown in Fig. 5(c).

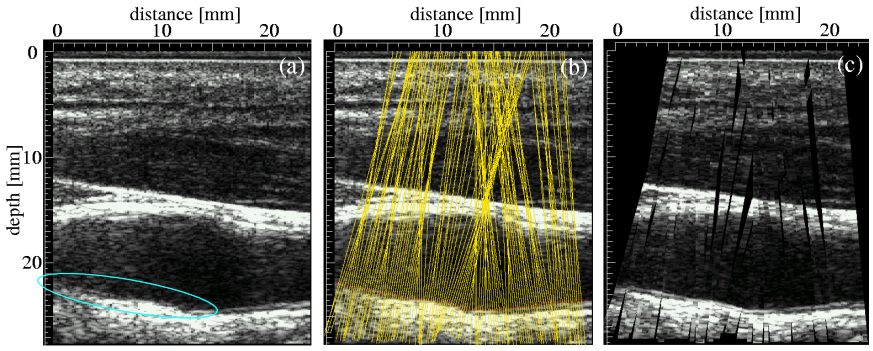

Fig. 5. (a) B-mode image obtained by conventional linear scanning. (b) Assigned posterior wall surface (red line) and calculated beams (yellow lines) superimposed on B-mode image of (a). (c) B-mode image obtained by the proposed method.

3.2. *Elasticity of extracted arteries measured* in vitro *and tissue characterization*

Figure 6(a) shows an elasticity image measured *in vitro*, and Fig. 6(b) shows the pathological image of the corresponding section. Lipids, blood clots, and fibrous tissue are indicated by yellow, red, and blue dashed lines, respectively. In Fig. 6(c), the elasticity image was classified based on the Mahalanobis distance between a single elasticity value of a pixel and the elasticity distribution of each tissue. In Fig. 7, the elasticity image was classified based on the likelihood between the elasticity distribution of each small region (not a single pixel) and that of each tissue. In comparison with the result of the classification based on a single elasticity value shown in Fig. 6(c), misclassified regions were reduced using the likelihood function between elasticity distributions as shown in Fig. 7. Figure 8 shows the tissue classification image obtained by analyzing the pathological image. The pathological image was analyzed as follows: The entire pathological image, which corresponds to the entire elasticity image, is divided into the M sections in the longitudinal direction of the arterial wall, and each m-th section of the M sections is divided into N_m regions in the arterial radial direction. Then, each region is classified into lipids, blood clots, fibrous tissue,

and calcified tissue based on RGB values in each region in the pathological image [13]. The regions classified as lipids, blood clots, fibrous tissue, and background were stained yellow, red, blue, and gray, respectively.

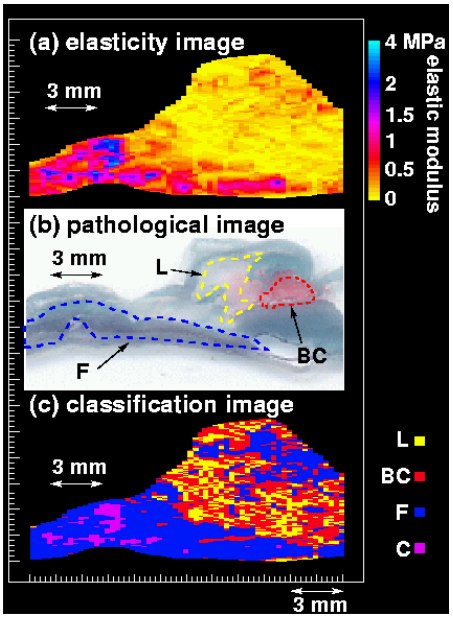

Fig. 6. (a) Elasticity image. (b) Corresponding pathological image. (c) Classification results based on the elasticity value of each pixel.

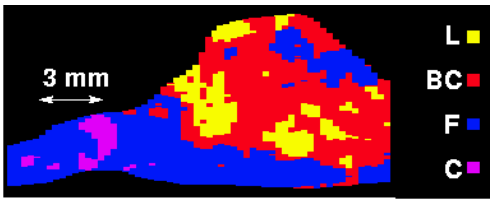

Fig. 7. Classification results based on the elasticity distribution of each small region.

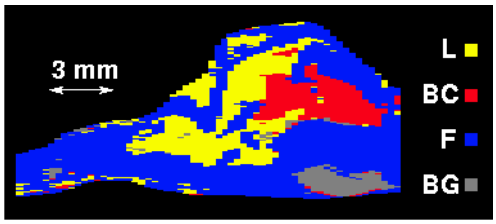

Fig. 8. Classification results based on the pathological image.

The correctness of the classification of each pixel was evaluated by comparing tissue classification images shown in Figs. 6(c) and 7 with that in Fig. 8 based on the pathological image. Using the likelihood, pixels classified into lipids was found to cluster, and correctly classified pixels were increased (lipids: 32.9%, blood clots: 21.0%, fibrous tissue: 72.8%) in comparison with classification based on a single elasticity value (lipids: 32.9%, blood clots: 17.4%, fibrous tissue: 64.2%).

3.3. In vivo *lateral motion estimation in carotid artery*

Figure 9 shows B-mode images of the same carotid artery of a 23-year-old healthy male. In the initial frame (at 0 s), the region of interest (ROI) was manually assigned as shown in Fig. 9(a). As shown in Fig. 9, the scan plane was almost parallel to the longitudinal direction of the artery. Therefore, in this case, the estimated axial and lateral displacements correspond to motions in the radial and longitudinal direction of the artery.

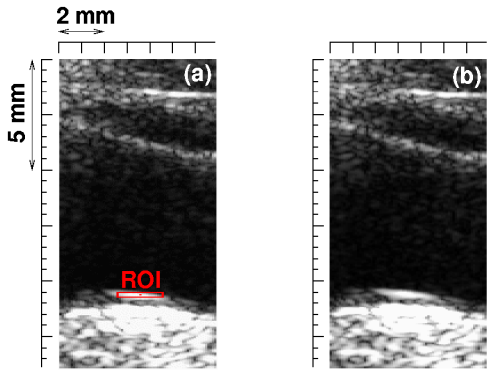

Fig. 9. B-mode images of a carotid artery. (a) At 0 s. (b) At 52 ms.

Figure 10(a) shows the electrocardiogram, and Figs. 10(b) and 10(c) show the estimated lateral and axial displacement, respectively. In Fig. 10(b), the estimated lateral displacement was much improved by increasing the number of interpolated RF lines whereas the estimation of the axial displacement was not influenced. Figure 11 shows the relationship between the longitudinal and radial displacements during cardiac cycles. In cardiac systole, the posterior wall moves in the depth direction due to the diameter expansion, and it moves toward the heart. Such a longitudinal motion of the artery was considered to be due to the motion of the heart and not due to blood flow because blood flows in the distal direction in systole (opposite to the estimated displacement).

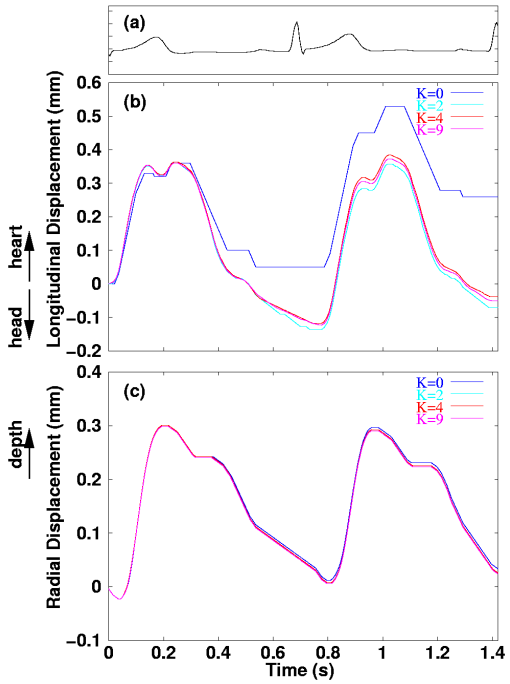

Fig. 10. (a) Electrocardiogram. (b) Estimated longitudinal displacement of the arterial wall. (c) Estimated radial displacement.

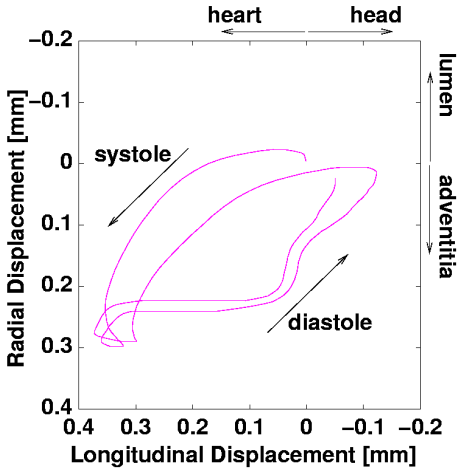

Fig. 11. Relationship between the longitudinal and radial displacements during cardiac cycles.

4. Conclusion

In this study, methods were proposed for accurate imaging of the carotid sinus which cannot be assumed as a straight cylindrical shell, measuring mechanical properties of the arterial wall based on the axial motion estimation, and detailed analysis of the artery motion based on the lateral motion estimation. Such methods for detailed analysis of the morphology and dynamic mechanics of the artery have potential for providing useful information on diagnosis of atherosclerosis.

References

[1] Moreno PR, Falk E, Palacios IF, Newell JB, Fuster V, and Fallon JT. Macrophage infiltration in acute coronary syndromes. Implication for plaque rupture. *Circulation* **90**, 775-778, 1994.
[2] Little WC, Constantinescu M, Applegate RJ, Kutcher MA, Burrows MT, Kahl FR, and Santamore WP. Can coronary angiography predict the site of a subsequent myocardial infarction in patients with mild-to-moderate coronary artery disease? *Circulation* **78**, 1157-1166, 1988.
[3] Loree HM, Kamm RD, Stringfellow RG, and Lee RT. Effects of fibrous cap thickness on peak circumferential stress in model atherosclerotic vessels. *Circ Res* **71**, 850-858, 1992.
[4] Falk E, Prediman K, Shah PK, and Fuster V. Coronary plaque disruption. *Circulation* **92**, 657-671, 1995.
[5] Brown G, Albers JJ, Fisher LD, Schaefer SM, Lin JT, Kaplan C, Zhao XQ, Bisson BD, Fitzpatrick VF, and Dodge HT. Regression of coronary artery disease as a result of intensive lipid-lowering therapy in men with high levels of apolipoprotein B. *N Engl J Med* **323**, 1289-1298, 1990.
[6] Shepherd J, Cobbe SM, Ford I, Isles CG, Lorimer AR, Macfarlane PW, McKillop JH, and Packard CJ. Prevention of coronary heart disease with pravastatin in men with hypercholesterolemia. *N Engl J Med* **333**, 1301-1307, 1995.
[7] Hallock P. Arterial elasticity in man in relation to age as evaluated by the pulse wave velocity method. *Arch Int Med* **54**, 770-798, 1934.
[8] Peterson RH, Jensen RE, and Parnell R. Mechanical properties of arteries *in vivo*. *Circ Res* **8**, 622-639, 1960.
[9] Mashiyama T, Hasegawa H, and Kanai H. Designing beam steering for accurate measurement of intima-media thickness at carotid sinus. *Jpn J Appl Phys* **45**, 4722-4726, 2006.
[10] Kanai H, Sato M, Koiwa Y, and Chubachi N. Transcutaneous measurement and spectrum analysis of heart wall vibrations. *IEEE Trans Ultrason Ferroelect Freq Contr* **43**, 791-810, 1996.

[11] Hasegawa H, Kanai H, Hoshimiya N, and Chubachi N. Evaluating the regional elastic modulus of a cylindrical shell with nonuniform wall thickness. *J Med Ultrasonic* **31**, 81-90, 2004.
[12] Kanai H, Hasegawa H, Ichiki M, Tezuka F, and Koiwa Y. Elasticity imaging of atheroma with transcutaneous ultrasound: preliminary study. *Circulation* **107**, 3018-3021, 2003.
[13] Inagaki J, Hasegawa H, Kanai H, Ichiki M, and Tezuka F. Construction of reference data for tissue characterization of arterial wall based on elasticity images. *Jpn J Appl Phys* **44**, 4593-4597, 2005.
[14] Inagaki J, Hasegawa H, Kanai H, Ichiki M, and Tezuka F. Tissue classification of arterial wall based on elasticity image. *Jpn J Appl Phys* **45**, 4732-4735, 2006.
[15] Numata T, Hasegawa H, and Kanai H. Measurement of longitudinal displacement of arterial wall based on cross correlation between interpolated ultrasonic RF echoes. In *Book of Abstracts of International Symposium on Bio- and Nano-Electronics*, Sendai, 73-74, 2006.